Bio-Design and Manufacturing (2020) 3:175–188
https://doi.org/10.1007/s42242-020-00078-4

RESEARCH ARTICLE

Bioprinting of novel 3D tumor array chip for drug screening

Mingjun Xie[1,2] · Qing Gao[1,2] · Jianzhong Fu[1,2] · Zichen Chen[1,2] · Yong He[1,2]

Received: 11 April 2020 / Accepted: 5 May 2020 / Published online: 19 May 2020

Abstract

Biomedical field has been seeking a feasible standard drug screening system consisting of 3D tumor model array for drug researching due to providing sufficient samples and simulating actual in vivo tumor growth situation, which is still a challenge to rapidly and uniformly establish though. Here, we propose a novel drug screening system, namely 3D tumor array chip with "layer cake" structure, for drug screening. Accurate gelatin methacryloyl hydrogel droplets (~0.1 μL) containing tumor cells can be automatically deposited on demand with electrohydrodynamic 3D printing. Transparent conductive membrane is introduced as a chip basement for preventing charges accumulation during fabricating and convenient observing during screening. Culturing chambers formed by stainless steel and silicon interlayer is convenient to be assembled and recycled. As this chip is compatible with the existing 96-well culturing plate, the drug screening protocols could keep the same as convention. Important properties of this chip, namely printing stability, customizability, accuracy, microenvironment, tumor functionalization, are detailly examined. As a demonstration, it is applied for screening of epirubicin and paclitaxel with breast tumor cells to confirm the compatibility of the proposed screening system with the traditional screening methods. We believe this chip will potentially play a significant role in drug evaluation in the future.

Keywords 3D tumor array chip (3D-TAC) · Gelatin methacryloyl (GelMA) · Drug screening · In vitro model · Bioprinting

Introduction

Together with surgery and radiotherapy, chemotherapy has become one of the three most effective methods to treat tumors [1]. Thousands of antitumor drugs are discovered and analyzed every year. That brings big challenges to current antitumor drug screening technology. In terms of tumor model for drug screening, two requirements of great concern are anticipated: (1) similar tumor morphology and microenvironment to that in vivo and (2) precise and scalable manufacturing method for the establishment of tumor models.

Regarding requirement (1), currently, most of the drug screening protocols are still based on two-dimensional (2D) cultures of tumor cells, which cannot simulate the three-dimensional (3D) tumor morphology in vivo, thus leading to weak clinical drug performance [2, 3]. Recently, with the development of microencapsulation [4–8], in vitro 3D tumor models based on hydrogels have been developed to provide a superior basis for antitumor drug screening [9, 10]. 3D structure reproduces the obstruction effect on the diffusion of drug molecules caused by extracellular matrix and outer layer of cells. Furthermore, 3D microenvironment in vitro can mimic the in vivo conditions [11] where the tumor cells are strictly regulated by the surrounding cells, extracellular matrix (ECM) molecules and biologic factors. These properties greatly increase the veracity of the tumor model and the reliability of the outcomes of the drug evaluation.

Among all biomaterials, gelatin methacryloyl (GelMA) hydrogel has become a widely used material in biofabrication [12–18], due to its capabilities of promoting cellular functionalization [19] and rapid crosslinking [20, 21]. This hydrogel is synthetized from the mammalian gelatin

Electronic supplementary material The online version of this article (https://doi.org/10.1007/s42242-020-00078-4) contains supplementary material, which is available to authorized users.

✉ Jianzhong Fu
fjz@zju.edu.cn

✉ Yong He
yongqin@zju.edu.cn

1 State Key Laboratory of Fluid Power and Mechatronic Systems, School of Mechanical Engineering, Zhejiang University, Hangzhou 310027, China

2 Key Laboratory of 3D Printing Process and Equipment of Zhejiang Province, School of Mechanical Engineering, Zhejiang University, Hangzhou 310027, China

degraded from the collagen [22–25], which plays an important role in guiding the metastasis and invade of tumor cells in vivo. Importantly, the stereolithographic method is of short duration and no residual curing conditions as enzyme and chemical crosslinking approaches. Accordingly, GelMA has great potential to be used to build 3D tumor models.

Regarding requirement (2), precise and scalable method for fabricating 3D tumor models is expected, which is the key success factor to affect the actual drug effect from the experimental data such as OD values. Furthermore, in the process of drug screening, we need lots of tumor models for different drug concentrations and repeated groups. Therefore, it is necessary to have appropriate method to establish 3D tumor arrays, rather than discrete tumor models. For example, microfluidic technology is capable to fabricate 3D models such as microspheres and microfibers. However, this technology can only fabricate exclusive 3D models. After the fabrication process, researchers have to transfer each tiny microsphere or microfiber into each culturing chambers of the culturing plates, respectively. It can be exceedingly inconvenient and time-consuming. More seriously, it could make the tumor cells stay outside the incubator for too long time. Thus, the significance of 3D tumor array emerges.

Confronted with this requirement, currently, the establishment of 3D cell-laden hydrogel array mainly depends on three approaches, namely crosslinking hydrogel with masks [26, 27], coating hydrogel on the prepatterned surface [28] and piezoelectric or thermal inkjet printing. However, their limitations cannot be ignored in actual applications. In the first method, the crosslinking light could scatter due to the Tyndall effect in the precursor solution, which leads to volumetric errors of the crosslinked models. Besides, the uncured bioink remains around the models and is difficult to clear up. In the second method, specifically manufactured membrane is needed and it cannot realize on-demand array printing conveniently. In the third method, the cell damage results from the instantaneous high pressure and temperature cannot be ignored [29]. Therefore, it is of great importance to develop an innovative strategy to establish reasonable in vitro 3D tumor array system for drug research.

In this study, a pioneering strategy for building in vitro 3D tumor array chip (3D-TAC) with "layer cake" structure is proposed (Fig. 1a, b, Fig. S2). The culturing chambers formed by stainless steel and silicon interlayer are convenient to be assembled and recycled. The printing units, GelMA microdroplets mixing tumor cells, are produced by high-voltage electric field force. The array distribution, size and cellular quantity of per model can be easily controlled by varying the route and duration program with upper computer. The transparent conductive membrane, which is common and inexpensive but never applied in chip establishment, is introduced in this strategy. When GelMA microdroplets with charges fall on it, the charges in droplets can be directly conducted away, avoiding charges to accumulate and droplets to mutually repel. Moreover, the transparent feature makes it easy to carry out a series of drug-testing items. To demonstrate the feasibility of this strategy, the droplet-forming process was fully analyzed. Three main factors, namely building tumor array on demand precisely, providing suitable microenvironment, containing tumor cell functionalization, were detailly assessed. It is worth mentioning that the encapsulated MDA-MB-231 breast tumor cells showed essential tumor characteristics, such as survival, spreading, metastasis and different cell cycle in 3D microenvironment. As a demonstration, we brought the novel 3D-TACs system into practical drug screening process to acquire all-round drug effect evaluation of epirubicin and paclitaxel, aiming to show the compatibility of the proposed drug screening system with the traditional screening methods, including laser scanning confocal fluorescence microscopy (LSCFM) observation (live/dead testing, tumor F-actin morphology), enzyme-linked immunosorbent assay (ELISA) examination (NAD+ examination for proliferation analysis, half maximal inhibitory concentration (IC50), vascular endothelial growth factor (VEGF) accumulative expression) and cellular apoptosis tested by flow cytometric (FCM) analysis. We conclude that this strategy can play a significant role in drug screening and contribute to the advancement of the field of tumor chemotherapy and other biomedical applications.

Materials and methods

Reagents and materials

High-voltage power (0–30 kV) was purchased from Dongwen, China. Stainless steel nozzles, 3D bioprinter, transparent conductive membrane, blue light source (405 nm, 3 W), nanowaterproofing spray reagent for nozzle lyophobic treatment, stainless steel plate and silicon interlayers were manufactured by Suzhou Intelligent Manufacturing Institution, China.

GelMA prepolymer solution was prepared by dissolving the freeze-dried GelMA (Suzhou Intelligent Manufacturing Institution, China) in modified eagle medium (DMEM, Hyclone, USA) at a concentration of 5% (w/v) containing lithium phenyl-2,4,6-trimethylbenzoylphosphinate (LAP, Suzhou Intelligent Manufacturing Institution, China) at a concentration of 0.5% (w/v). The GelMA prepolymer solution was filtered through a 0.22-μm filter for sterility before using. MDA-MB-231s breast tumor cell line, fluorescent staining kits and ELISA kits, fluorescein isothiocyanate-conjugated dextran (FITC-dextran, 10 kDa), collagenase II, fluorescent pellets, antitumor drugs (epirubicin and paclitaxel) were purchased from Tangpu, China. Dulbecco's phosphate-buffered saline (DPBS), trypsin (SH30042.01

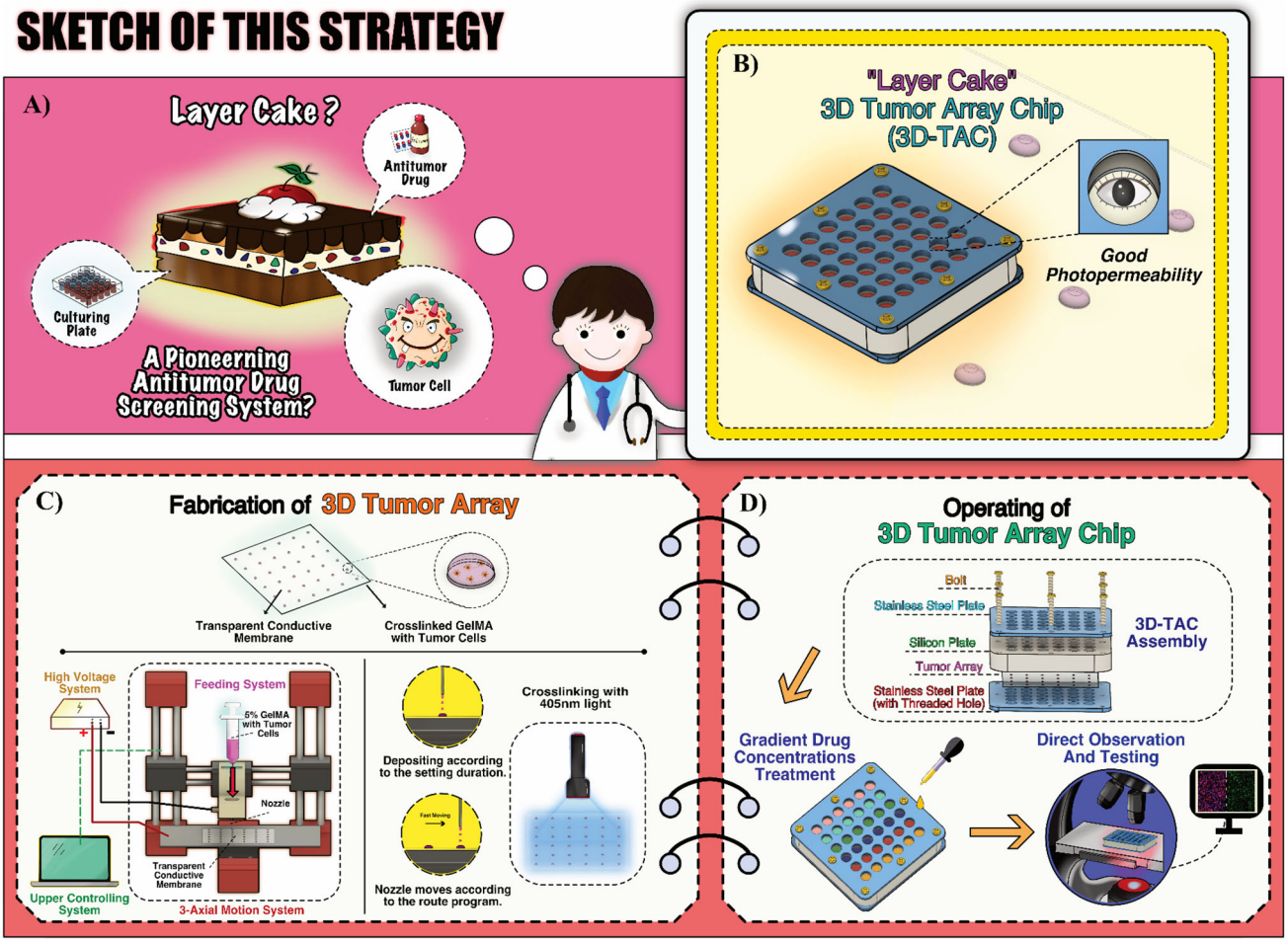

Fig. 1 Sketch of the pioneering strategy. **a** Inspiration of this strategy. Layer cake structure is considered to be used to build a new kind of 3D drug screening system. **b** Sketch of the "layer cake" 3D tumor array chip (3D-TAC). The transparent conductive membrane of 3D-TAC owns good photopermeability for further examinations. **c** Fabrication protocol of 3D-TAC. **d** Assembly and using method of 3D-TAC

0.25%), penicillin–streptomycin (100) were purchased from Hyclone, USA. Fetal bovine serum (FBS) was obtained from Procell, China. Complete medium was prepared by mixing DMEM, FBS (10% v/v) and penicillin–streptomycin (1% v/v).

Rheometer (TA Instrument, USA), LSCFM (OLYMPUS FLUOVIEW FV3000), scanning electron microscopy (SEM) and high-speed camera (pco. dimax S1), vacuum-drying machine, compressing test machine were provided by Suzhou Intelligent Manufacturing Institution, China. Microplate reader, automatic snapping microscope system and flow cytometer were supplied by Zhejiang University.

Printing device establishment and chip assembly

As illustrated in Fig. 1c, the metal plate on the 3D printer was connected with positive pole of the high-voltage power and the nozzle was grounded, forming high-voltage electric field. The transparent conductive membrane was placed on the metal plate. The environment was strictly controlled as 30 °C and 50% humidity. GelMA bioink was fed by the syringe pump on the 3D bioprinter. The 3D bioprinter was connected with the upper computer so that the movement of nozzle could be controlled. The 405-nm wavelength light was used for the crosslinking of GelMA array on the chip. After finishing the array fabricating and crosslinking, the membrane was assembled with the stainless steel and silicon plates. The system was screwed up by bolts as shown in Fig. 1d to form 3D-TAC for drug screening.

Droplet formation analysis

High-speed camera was used to record the formation process of droplets and different printing states. The frame rate was set at 100fps and the exposure time was 3227 μs. We set two nozzle sizes: 28G, 32G and three flow rates: 10 μL/min,

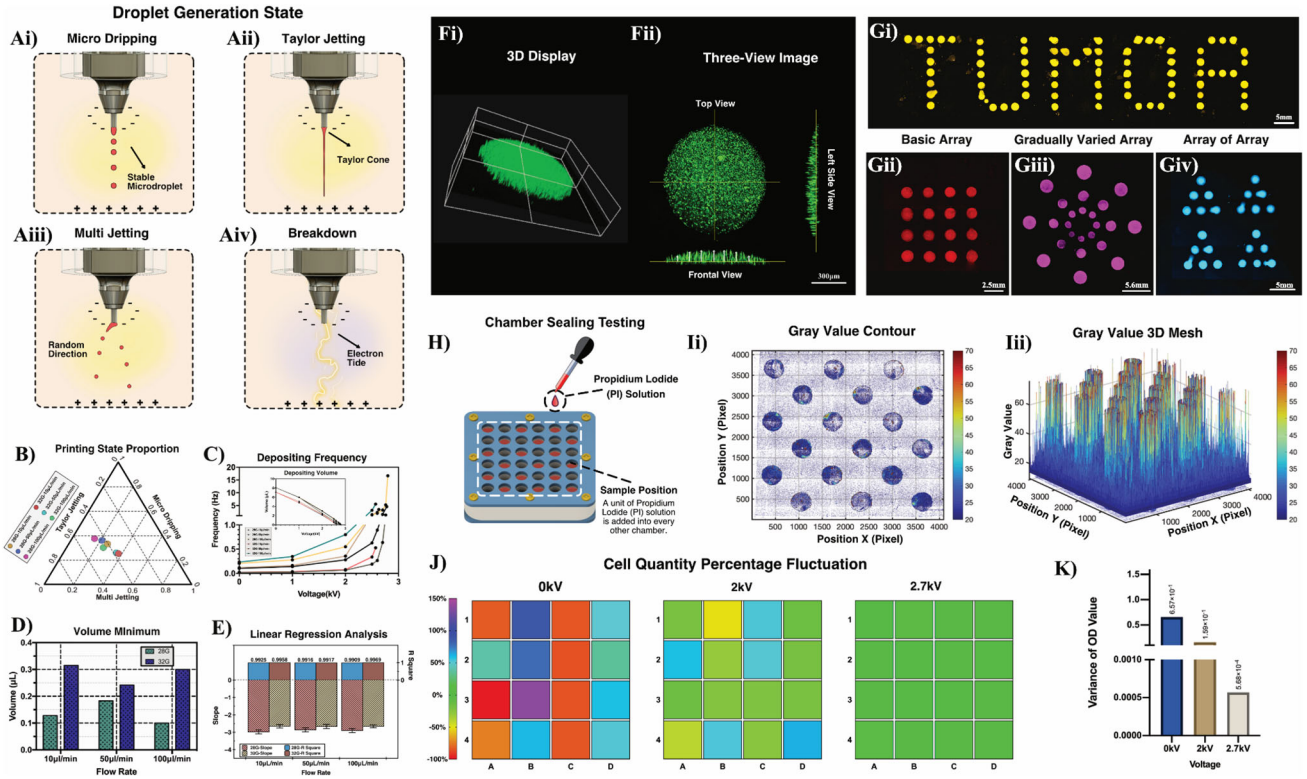

Fig. 2 Analysis of droplet formation process and 3D-TAC establishment feasibility. **A** Different printing states happening in the dropping process. (i) Microdripping. (ii) Taylor jetting. (iii) Multijetting. (iv) Breakdown. **B** Voltage proportions of per state. The intersection of the axes and parallel lines over data points is the proportions of the corresponding state. **C** Printing frequency and resolution and depositing volume. **D** Volume minimum. **E** Linear regression analysis. The bars above the line are R^2. The bars below the line are the slopes acquiring from linear regression analysis. **F** LSCFM images of 3D GelMA unit. (i) 3D display. (ii) Three-view images. **G** LSCFM images of ON-DEMAND GelMA arrays. (i) Character pixel art "TUMOR." (ii) Basic array. (iii) Gradually varied array. (iv) Array of array. **H** Sketch of chamber sealing testing experiment. **I** Gray value distribution of the PI image on the membrane. (i) Gray value contour. (ii) 3D mesh. **J** Heat maps of the cell quantity percentage fluctuating in per chamber. The percentage value is represented by color according to the legend besides. **K** Variance of the cell number fluctuating percentage

50 μL/min, 100 μL/min, to carry out orthogonal experiments under continuously changing voltage. The proportion of different printing was calculated with the formula (V_{boundary} was the exact voltage when state changed and $V_{\text{breakdown}}$ was breakdown voltage.):

$$\text{State proportion} = \frac{V_{\text{boundary}}}{V_{\text{breakdown}}} \times 100\% \tag{1}$$

From the recorded video, the lengths of short axis (Ds) and long axis (Dl) of the elongated droplet (Fig. 2Ci) and dropping frequency were measured by ImageJ software. The depositing volumes were transformed by frequency data and the corresponding flow rate. The depositing volume was calculated with the formula below, and the linear relationship between volume and voltage was analyzed with MATLAB software. (Q was the flow rate of the prepared bioink, and f was the generation frequency of the microdroplet.):

$$\text{Depositing volume} = \frac{Q}{60}/f. \tag{2}$$

Examination of the manufacturing feasibility

On-demand array printing: Researchers can establish on-demand arrays for specific goals with this method. On-demand arrays were printed with GelMA bioink mixed with fluorescent pellets. The arrays were fabricated by 32G nozzle with 2.7 kV voltage and 10 μL/min flowrate. 3D shapes of the GelMA unit and on-demand printing array were captured with LSCFM.

Chamber sealing test: Propidium iodide (PI) solution was added in every other chamber of the assembled chip (Fig. 3C). After 96-h standing in dark place, the system was dried in super clean bench for 24 h. The chambers were imaged with LSCFM. The fluorescent intensity of the image was read and converted to gray value with MATLAB software.

Cell quantity fluctuation percentage: Here, GelMA bioink mixed with MDA-MB-231s (2×10^6 cells/mL) was applied to fabricate 4×4 3D-TACs under different voltage (0 kV, 2 kV, 2.7 kV) with 32G nozzle and 10 μL/min flowrate. Cell quantity in every sample can be reflected by optical den-

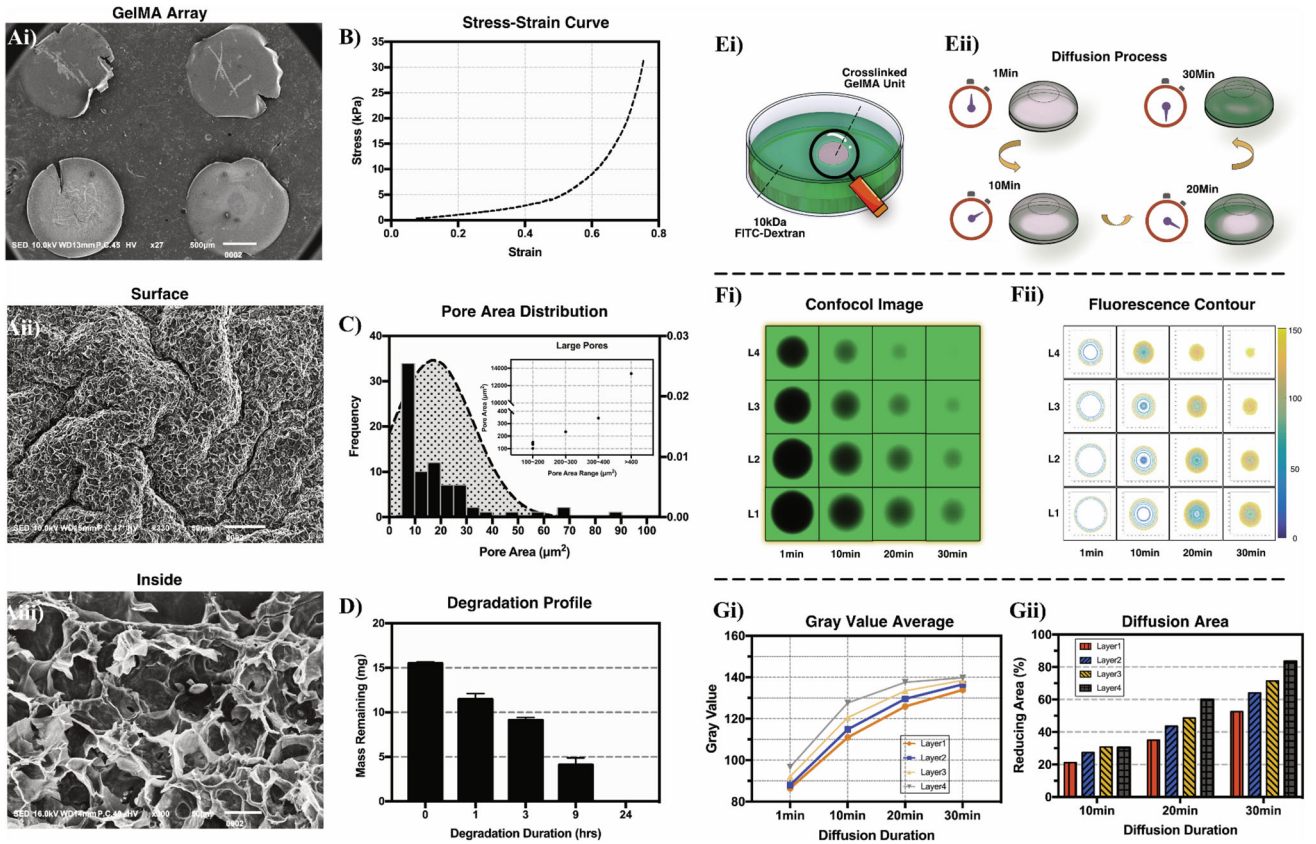

Fig. 3 GelMA ECM properties. **A** SEM images of GelMA array. (i) GelMA array. (ii) Surface. (iii) Inside. **B** Stress–strain curve. **C** Pore area distribution analyzed with GelMA inside SEM images. The smaller graph showed the pore areas of some larger pores. **D** Degradation profile of GelMA in 2U/mL collagenase II solution. **E** The sketch of the diffusion experiment. **F** Testing of diffusion effect in different layers and durations. (i) LSCFM images of FITC-dextran in GelMA unit. (ii) The contour graphs of the gray value data. **G** Quantitative analysis of the diffusion results. (i) The gray value averages of different layers and durations. (ii) The diffusion areas of different layers and durations

sity (OD) values tested by CCK-8. The quantity fluctuating percentage was calculated with the formula below and summarized in heat maps (OD(sample) was the OD value of sample. OD(blank) was the OD value of DMEM with CCK-8. OD(average) was the average OD value of all samples):

$$\text{Quantity fluctuating percentage } (\%) = \frac{\text{OD}\left(\text{sample}\right) - \text{OD}\left(\text{average}\right)}{\text{OD}\left(\text{average}\right) - \text{OD}\left(\text{blank}\right)} \times 100\%. \quad (3)$$

Characterization of GelMA-based ECM

Rheological examination. Here, we carried out the shear-thinning feature, loss/storage modules varying with time varying and temperature varying. The GelMA bioink tested by 400-mm testing rotor was chosen. The shear-thinning test was carried out at the temperature of 30 °C. The temperature-varying examination was carried out at the temperature range of 1–31 °C. The time-varying examination was carried out at the temperature of 30 °C, and the time range was 200 s.

SEM images of GelMA arrays: To examine the micromorphology of GelMA array, it was dried in vacuum-drying machine at − 80 °C for 24 h. Then, samples were treated with a metal spraying machine and observed under SEM. The inner morphology images were imported into ImageJ software, and the pore areas were analyzed. The area frequency distribution and the normal distribution data were calculated.

Compressing and degradation testing: Matrix elasticity and degradation profiles can strongly affect the tumor growth. Here, GelMA cylinders was fabricated by a Ø9 mm × 6.3 mm mold. Then, the crosslinked GelMA was compressed under a stress–strain curve testing machine. Another group of GelMA cylinders were fabricated by a Ø9 mm × 2 mm mold. Then they were immersed in 1.5 mL DPBS containing 2 U/mL collagenase II and incubated in incubator at 37 °C with 5% CO_2. The degradation durations were set as 0, 1, 3, 9, 24 h (three repeated samples). The samples were taken out

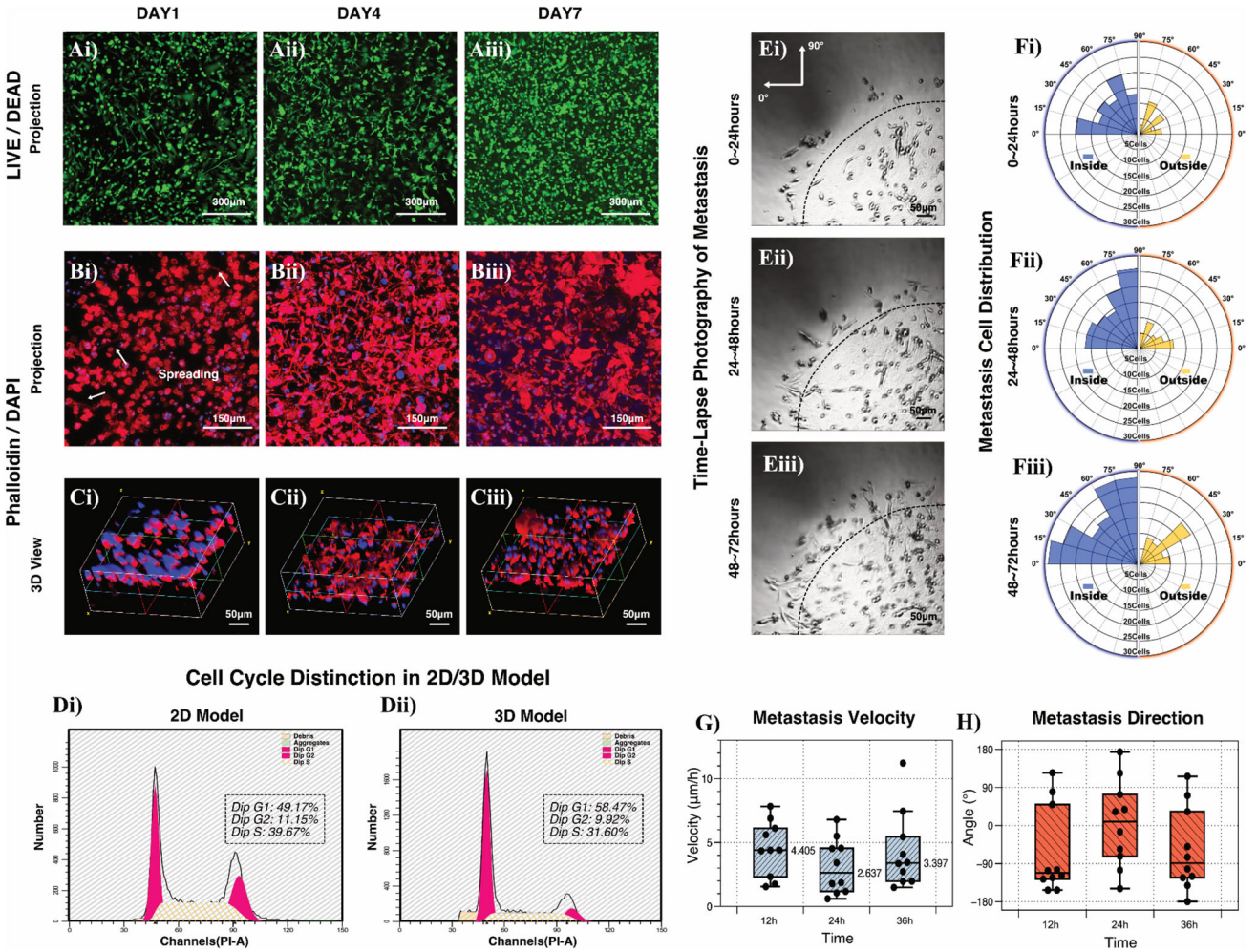

Fig. 4 Growth state of breast tumor cells in 3D-TAC. **A** LSCFM images of live/dead staining of the MDA-MB-231s encapsulated in 3D-TAC (projection). (i) 1 day. (ii) 4 days. (iii) 7 days. **B** LSCFM images of F-actin/nucleus markers of the MDA-MB-231s encapsulated in GelMA 3D-TAC (projection). (i) 1 day. (ii) 4 days and (iii) 7 days. **C** LSCFM images of F-actin/nucleus markers from the MDA-MB-231s encapsulated in GelMA 3D-TAC (3D view). (i) 1 day. (ii) 4 days and (iii) 7 days. **D** FCM analysis of cell cycle distinction in 2D and 3D models. (i) 2D model. (ii) 3D model. **E** Metastasis images of MDA-MB-231s in GelMA. (i) 0–24 h. (ii) 24–48 h. (iii) 48–72 h. **F** Metastasis MDA-MB-231s quantity distribution. The circle radius represents the quantity of cell. (i) 0–24 h. (ii) 24–48 h. (iii) 48–72 h. **G** Metastasis velocity from 0 to 36 h. **H** Metastasis direction from 0 to 36 h

at planned duration. Remove the liquid and the samples were transferred into the vacuum-drying machine at − 80 °C for 24 h. Then, the masses of the dried samples were weighed, respectively. The data were presented as the mean ± SD of measured record.

FITC-dextran diffusion analysis: To examine the controlled diffusion capability of GelMA array, it was immersed in the DPBS containing 300 μg/mL FITC-dextran (Fig. 4Ei, ii) and observed under LSCFM with Z-stack function. The images were captured at every 1 min after immersing for 1 h with the same capturing parameters. The captured images of four layers at 1 min, 10 min, 20 min, 30 min were transformed to grayscale images and plotted with MATLAB software. Furthermore, the diffusion areas were analyzed with ImageJ software.

Tumor growth state in 3D-TACs

Fabrication of 3D-TACs encapsulating MDA-MB-231s: The MDA-MB-231s were detached and resuspended in the prepared GelMA bioink to a concentration of 8×10^6 cells/mL and 2×10^6 cells/mL (for metastasis observation). The 3D-TACs were fabricated by 32G nozzles with 2.7 kV voltage and 10 μL/min flowrate and crosslinked by 405-nm wavelength light. The systems were cultured with complete medium in 5% CO_2 at 37 °C.

Cell viability: The survival rates of MDA-MB-231s in 3D-TACs were measured after 1-, 4-, 7-day culturing to examine. The samples were treated with Calcein-AM/PI kits for 30 min and washed by DPBS. Then, the chips were observed under LSCFM by acquiring two images of each frame: green for

live cells and red for dead cells, respectively. The live and dead cell quantifications were performed with ImageJ software, and cell viability was calculated as the ratio of the number of live cells to the total number of cells.

Cell spreading: MDA-MB-231s morphology was observed after 1-, 4-, 7-day culturing to examine the cell spreading capability. The samples were treated by TRITC phalloidin for 30 min and DAPI for 5 min for cell cytoskeleton dyeing, including F-actin and nucleus. At last, the chips were imaged with LSCFM.

Cell cycle: MDA-MB-231s were cultured in the proposed 3D-TAC and conventional 96-well culturing plate (5000 cells/well) for 5 days. After that, the cells in two kinds of models were detached and fixed with 4% paraformaldehyde (PFA) and stained with cell cycle detecting kit. Then, the cell cycles were detected by FCM and analyzed with FlowJo software.

Cell metastasis: The metastasis process in 72 h of MDA-MB-231s in GelMA array was recorded with automatic snapping microscope system. The cells in every 15° directions inside and outside of the structure were counted with ImageJ software. Ten cells were chosen to carry out path tracking from 0 to 36 h. The metastasis velocity was calculated with the formula below (S was the metastasis distance):

$$\text{Metastasis velocity} = \frac{S}{24} \times 100\%. \tag{4}$$

Drug screening with 3D-TACs and conventional well plate

Screening models establishment and drug preparation: 3D-TACs encapsulating MDA-MB-231s (2×10^6 cells/mL, 32G, 10μL/min, 2.7 kV) and conventional 96-well plate seeded by MDA-MB-231s (5000 cells/well) were established as 3D and 2D tumor models, respectively. Epirubicin (noncell cycle specificity drug) and Paclitaxel (cell cycle specificity drug) were diluted with the complete medium.

Live/dead examination: This part was aimed at not only viability testing but also rough screening to determine an approximate dose range. After 24-h culturing, epirubicin at the concentration of 0 μM, 0.01 μM, 1 μM, 100 μM was added into 4 repeat samples, respectively. The testing durations were set as 24, 48, 72 h. At the testing time, the samples were treated with Calcein-AM/PI kits for 30 min and washed by DPBS. Then, the chips were observed under LSCFM and analyzed viability with ImageJ software.

VEGF accumulative expression: The concentrations of epirubicin and paclitaxel were set as 0 μM, 1 μM, 5 μM, 10 μM, 25 μM, 50 μM. Transfer 100 μL cell supernatant in every chamber into ELISA plate after 1, 2, 4 days of culturing and incubate for 2 h. Clean up the plate and add the reagents of the VEGF detecting kit in sequence. Then, read OD value (450 nm and 630 nm) with the microplate reader and the corresponding mass of VEGF was calculated by MATLAB software according to the standard VEGF curve.

NAD+ examination for proliferation and IC50 conduction: 3D and 2D models and the drug doses were set as above. Samples after 120-h culturing were immersed in CCK-8 kit (10% v/v) for 3 h and read OD values (450 nm) by microplate reader. The results were initialized according to the 0 μM group. IC50 was analyzed with the standardized data by calculating the concentrations at 50% spot of the OD value curves with MATLAB software.

Tumor morphology: 3D models and the drug doses were set as above. After 7-day drug treatment, the samples were stained by TRITC phalloidin and DAPI for 30 min and 5 min, respectively, and were imaged with LSCFM. After imaging, all the images acquired by Z-stack function were projected to a single image.

Tumor apoptosis by FCM: The 3D and 2D models and the drug doses were set as above. Cells in two kinds of models were detached after 72-h culturing and stained with cell apoptosis detection kit (Annexin V/PI) and examined by FCM. The detecting particles count was set as 1×10^4. Four cellular distributions were divided by FlowJo software according to the nonstained cells group. The distributions were interpreted as below: Annexin V−/PI−: live cells. Annexin V+/PI−: early apoptosis cells. Annexin V+/PI+: late apoptosis/dead cells. Annexin V−/PI+: dead cells.

Results and discussion

Parametric effect on microdroplet formation

Printing states: Under the high-speed camera, with the increasing of voltage, four different printing states were observed, which were significant for choosing the most suitable printing state for this strategy (Fig. 2Ai–iv, Fig. S1). Microdripping: When lower voltage was applied, dispersive droplets were generated because the electric field force provided an auxiliary force to break up the surface tension for gravity. This state is the most important for 3D-TAC establishment due to its high controllability and stability. Taylor jetting: When the voltage increased, Taylor cone formed around the nozzle and a continuous jetting vertically shot down. Because of the short distance between the nozzle and the membrane, there was not enough time for the evaporation of the aqueous phase. That prevented the appearance of Coulomb fission phenomenon [30, 31] and the liquid could not break up into smaller droplets (Supplementary information, additional discussion). Multijetting: With the increase of voltage, the Taylor cone became unstable. It shook around the nozzle and unstable droplets were generated, which is unexpected in the 3D-TAC construction process. Breakdown:

When much higher voltage was applied, the air between the nozzle and the membrane was disrupted. Bright light occurred in the printing area intermittently, which should be strictly avoided.

Proportions and boundary conditions: As shown in Fig. 2Bi, ii, the critical voltage, which is the voltage boundary between microdripping state and Taylor jetting state, was lower when a smaller nozzle size was used, but the influence of flow rate was not obvious. Moreover, the breakdown voltage was higher when a smaller nozzle size was used. The voltage proportions of every states before breakdown are displayed in Fig. 2Biii. The proportions of microdripping state, which is important in 3D-TAC establishment process, were all above 25% with all groups of parameters. This finding confirmed that there was enough controllable voltage range for stable construction of the array.

Liquid shape around nozzle. In microdripping state, when the voltage grew to a certain value, its upper end began to be stretched and the neck became narrower, which accelerated the separation of the droplets. Here, Ds and Dl of the elongated droplet are summarized in the bubble chart shown in Fig. 2Ciii. These data revealed that the values of Ds and Dl were both higher in larger nozzle size group. It was because when droplet flows out from nozzle, liquid tended to fill the nozzle tip and remains there by surface tension. For larger nozzle, the excluded droplet could remain there and keep for a larger volume. However, the values did not show noticeable differences among different flow rate groups, while both Ds and Dl got smaller with the increase of voltage. In addition, Fig. 2Cii illustrates that with the increase of voltage, the ratio of Ds/Dl reduced in that the elongation effect in the high-voltage electric field was stronger.

Frequency and resolution. *Droplet* volume is important for its influence on model size and cell quantity. As shown in Fig. 2Di, the deposition frequency was higher when higher voltage was applied. The single droplet volume transformed by the frequency data is shown in Fig. 2Dii. The minimum volume could reach around 0.1 μL (Fig. 2Diii). Furthermore, the volume-voltage lines showed nearly linear relationship because all the values of R^2 were above 0.99 (Fig. 2Div). In addition, the slope data showed that when the same flow rate was used, the decreasing speed was higher in larger nozzle size group. This result is important for the control of the single droplet volume in chip establishment.

Feasibility of 3D-TAC establishment process

The strategy presented in this paper is aimed at establishing the on-demand construction of 3D-TAC. Regarding the manufacturing process, four significant problems should be considered: (1) the 3D growth environment structure. (2) The feasibility of on-demand droplet array printing. (iii) Chamber independence. (iv) Uniformity of the cell number among samples.

3D growth environment: As displayed in Fig. 3Ai, ii, GelMA unit had an arched shape on the membrane, which established a 3D growth environment for encapsulated tumor cells after crosslinking. Additionally, the arched shape provides a gradually varying thickness, which was suitable for material exchanging between the inner and outer space of hydrogel.

On-demand array printing: The printing route and depositing duration could be easily modified by the default programs in upper computer. Thus, not only could the strategy be used to fabricate a basic array (Fig. 3Bii), but also to build character pixel art (Fig. 3Bi). Furthermore, simply by means of setting different linger time or repeating a specific G-code group, more complex arrays could be directly developed, such as "gradually varying arrays" (Fig. 3Biii) and "array of array" (Fig. 3Biv) without preparing special mold or mask. This strategy made it possible to obtain on-demand 3D-TAC for a series of particular drug screening requirements.

Chamber sealing of 3D-TAC: The independence of per culturing chamber must be guaranteed; otherwise, the drugs at different concentrations may diffuse toward each other. As shown in the gray value data graph (Fig. 3Cii, iii) converted from Fig. S3, the contour and mesh image displayed a clear profile in the chambers placing PI solution. This indicated that the PI remained in the presupposed chambers, which was evidence of a qualified sealing of the 3D-TAC.

Cell quantity fluctuating percentage: Low cell initial quantity fluctuation in per chamber is significant to ensure the screening accuracy. The cell quantity fluctuating percentage range (represented by color) in 4 × 4 3D-TAC of 0 kV, 2 kV, 2.7 kV was − 99.5 to 136.0%, − 51.0 to 62.6%, − 4.6 to 3.1%, respectively, and the variance was 0.657, 0.159, 0.000568 (Fig. 3E, F). This illustrated that the fluctuation percentages were quite different in 0 kV group but were clearly improved with the increase of voltage. This was due to the size change of the microdroplet caused by the electric field varying. In the results above, single droplet volume has been measured. The cell number in every droplet could be calculated by multiplying the single droplet volume and the applied cell density of bioink. However, when lower or no voltage was applied, droplet accumulated around the nozzle for a longer time and formed larger droplets. During the printing process, there was no or little droplet dropping on the conductive membrane at some setting spots, but too much at others, which led to low uniformity in the cell count. In contrast, when the voltage was increased, the droplet size decreased and the deposition frequency increased. This resulted in higher printing resolution and made it possible to uniformly deposit a specific quantity of cells in every sample.

In conclusion, the analysis of manufacturing process of 3D-TAC indicated that the proposed strategy was with high customizability, feasibility and accuracy for drug screening.

GelMA ECM characterization

Since the microenvironment created by hydrogel has a great influence on tumor cells growth, the material properties were examined in detail.

Rheological testing: The rheological property of uncured bioink is significant in that it would influence the printing process and cellular microenvironment formation. According to Fig. 4J, the shearing thinning (30 °C) of GelMA was obviously displayed and the viscosity was low. Furthermore, the loss/storage modulus variation with the temperature changing was tested, which was important to determine the gelation point. As shown in Fig. 4H, two curves were crossed at the point of around 20.5 °C (gelation point), which was much far from the chosen printing temperature. Thus, the droplet could be stably generated and the crosslinked GelMA ECM would be more uniform. Time varying was another important property because GelMA is a kind of noncrystal. With time going, the state of GelMA could gradually change. To justify the stability at the chosen printing temperature (30 °C), the loss/storage modulus variation with time changing was tested. As shown in Fig. 4I, two curves were both relatively plain and retain a relatively stable interval in testing period. This result indicated that uncured GelMA could contain stable liquid phase and form consistent ECM after irradiation.

SEM morphology: The SEM images shown in Fig. 4Ai–iii revealed numerous micropores forming after crosslinking, indicating the GelMA ECM allowed the material exchange between the inner and outer environment of the structure. Noticeably, the surface pores were much smaller and denser than the inner ones. This phenomenon, as discussed in our earlier research [32], resulted from the difference of crosslinking conditions. The inner pore areas smaller than 100 μm^2 nearly followed a normal distribution, and the average was 493.277 μm^2 (Fig. 4C). It is worth mentioning that there were a few larger pores formed during the crosslinking process. The area even reached nearly 1.4×10^4 μm^2. Thus, it was convenient for tumor cells to spread inside the GelMA 3D model like in vivo situations.

Stress–strain curve: Matrix dynamics is critical for tumor growth. Previous researching has demonstrated that the elastic modulus of malignancy could be up to 20 kPa. Specifically, the peak of breast malignancy elastic modulus can occur at 0.31–0.75 kPa, 1.54–1.99 kPa and 5.75 kPa [33]. Here, the elastic modulus of 5% GelMA was 4.322 ± 1.739 kPa, showing promising elasticity (Fig. 4B). This modulus was exactly in the range of the one referred above. Remarkably, we chose the GelMA with a low methacrylation level in this work for obtaining more suitable microenvironment. Accordingly, its elasticity was lower than that of the GelMA with high methacrylation level [21].

Degradation profile: GelMA has been reported that its degradation profile can be modified by tuning the concentration [21]. Here, the degradation profile of the applied 5% GelMA was tested with collagenase II [21, 34]. The results of the test shown in Fig. 4D revealed that the samples were completely degraded within 24 h, suggesting that GelMA had the ability of responding to a biologic environment.

Molecule diffusion: The diffusion images of GelMA encapsulating FITC-dextran for 1, 10, 20 and 30 min are shown in Fig. 4Fi. The transformed gray-level contour graphs (Fig. 4Fii) revealed that with the increase of immersing duration, the fluorescent molecules gradually invaded the GelMA unit. Moreover, the finishing speed of the overall diffusion at the upper layers was much higher than those at the lower layers (Fig. 4Gi, ii). This finding indicated that the GelMA sample could achieve the gradual drug diffusion as in vivo situation.

In summary, given its great porosity, ideal elasticity, excellent gradual molecular diffusion controllability and exceptional degradation profile, GelMA was considered worthy of being further explored in 3D-TAC establishment.

Growth state of MDA-MB-231s in 3D-TAC

Tumor cells experienced the electric field force in this strategy. For drug screening application, tumor cells encapsulated in 3D models should keep their fundamental functions before drug treatment. That would guarantee that the results only depend on drug concentration excluding mechanical injury.

Cell viability and spreading: The images of live/dead testing are shown in Fig. 5Ai, iii. The tumor cells showed high viability (above 90%, Fig. S7) even after exposing to the electric field force during the procedure. The morphology of MDA-MB-231s (Fig. 5Bi–Ciii) clearly illustrated the encapsulated MDA-MB-231s began to spread on the first day of culturing. On the 4th day, almost all the cells had spread in hydrogel with wider margin. On the 7th day, some tumor cells accumulated in GelMA becoming larger tumor-like growth.

Cell cycle: ECM can influence cell proliferation behavior. According to the FCM testing results (Fig. 5Di, ii), the second gap (G2) proportion of 3D models (9.92%) was lower than the one of 2D models (11.15%). This result illustrated that more MDA-MB-231s in 3D-TAC were preparing the synthesis of relating DNA and proteins instead of mitosis. This phenomenon resembled the situation in actual organism because of restriction deriving from the 3D extracellular matrix. The cell cycle distinction between the 2D and 3D models would be critical for the drug screening results because some antitumor drugs own cell cycle specificity. The appropriate 3D models as proposed 3D-TAC could provide more accurate screening conditions.

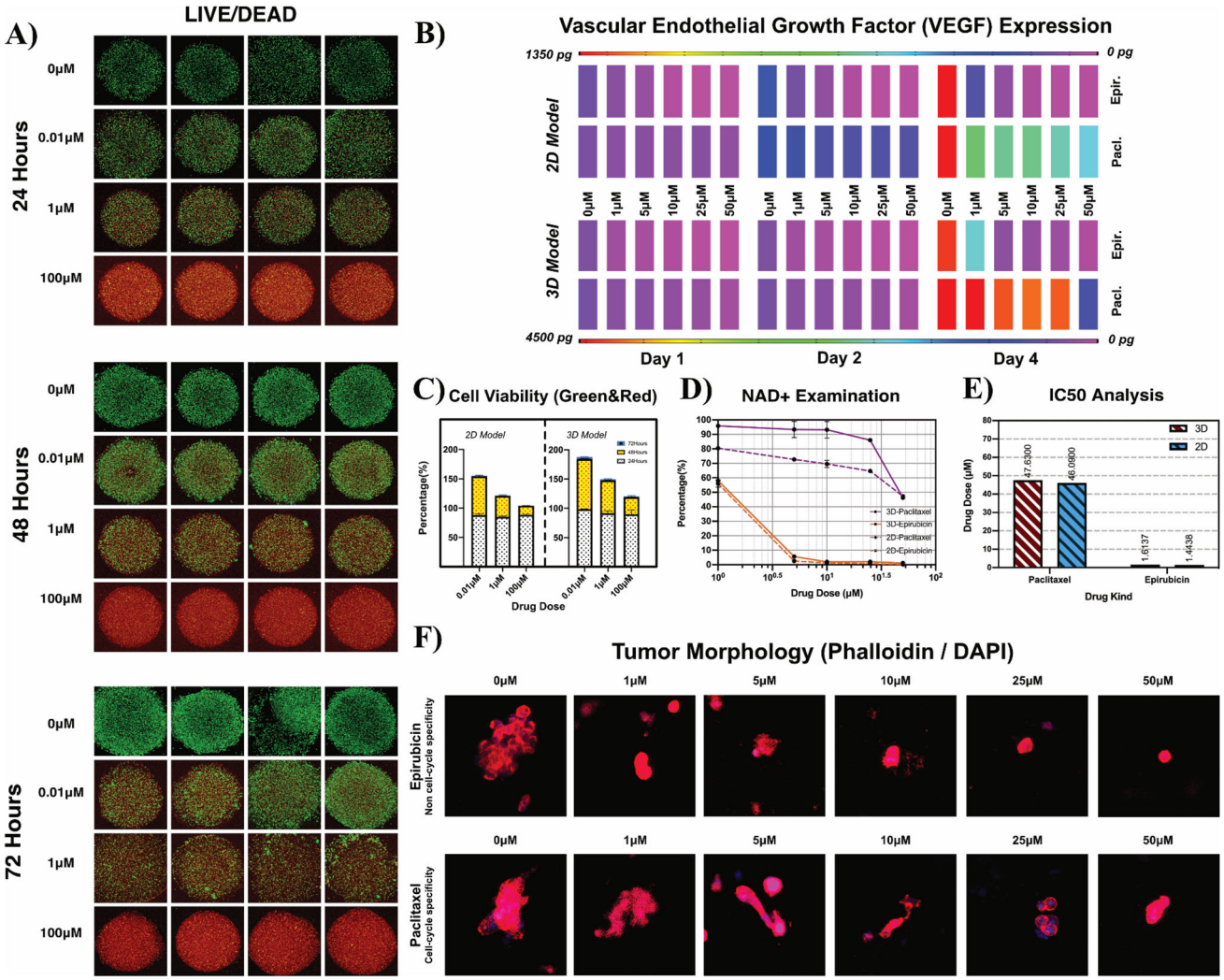

Fig. 5 Drug screening with 3D-TAC and conventional well plate (LSCFM and ELISA characterizations). **A** Drug effect (live/dead) of different treating duration. **B** VEGF accumulative expression mass of epirubicin (noncell cycle specificity) and paclitaxel (cell cycle specificity). **C** Viability calculated by the live/dead images. **D** NAD+ examination to reflect the proliferation situation. **E** IC50 analysis. **F** Tumor morphology (phalloidin/DAPI)

Metastasis process: The metastasis ability of tumor cells is significant for invasion and dissemination from primary solid tumors and for the building of lethal secondary metastases at distant organs [35–39]. During metastasis (Fig. 5Ei–iii), some cells encapsulated in the GelMA overcame the obstacle of the hydrogel network and escaped outside as in vivo *situation* (Fig. 6Ei–iii). Because the vertical height of the GelMA unit was gradually varied, the material interaction near the edge was more frequent. Cells tended to migrate there from the same or different layers and exited ECM. Additionally, cell tracks from 0 to 36 h were marked for kinematics analysis (Fig. S8). The velocity (Fig. 5G) and moving direction (Fig. 5H) were not uniform due to different pore sizes.

Together, these results indicated that MDA-MB-231s in 3D-TAC preserved their high viability, as well as their ability to spread and metastasize after undergoing the high voltage.

The above research led us to ponder over the additional applications of this strategy in the future. For instance, the kind of encapsulated cells in the chips could be extended. Besides tumor cells, a series of stem cells and somatic cells could be chosen as the model subjects, establishing "3D-xAC," such as "3D Stem Cell Array Chip," "3D Vessel Array Chip," "3D Liver Array Chip." Accordingly, this method not only could be applied for antitumor drug screening, but also for stem cell induction, somatic cell functionalization, etc. Moreover, the 3D-TACs (or other array chips) could be produced on a large scale and be cryopreserved for more convenient using. Researchers could easily acquire enough

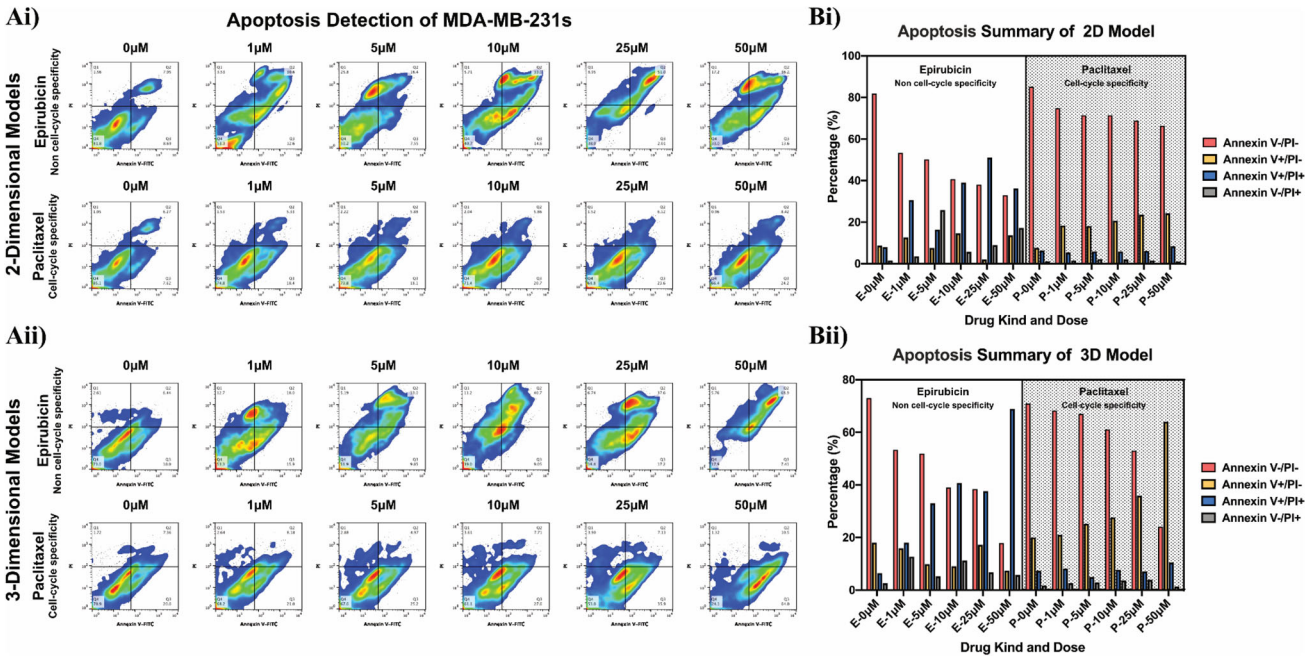

Fig. 6 Apoptosis of MDA-MB-231s (flow cytometric testing). **A** FCM analysis of tumor apoptosis treated by epirubicin and paclitaxel. (i) Common well plate (2D). (ii) 3D-TACs. **B** Summary of apoptosis phase. (i) Common well plate (2D). (ii) 3D-TACs. Annexin V−/PI−: live cells. Annexin V+/PI−: early apoptosis cells. Annexin V+/PI+: late apoptosis/dead cells. Annexin V−/PI+: dead cells

tumor models for new antitumor drug screening and assemble them with "layer cake" culturing plates directly. Altogether, this strategy has great potentials to be used in more biomedical applications.

Drug screening with 3D-TACs and conventional well plate

Epirubicin, a cell-permeable anthracycline antitumor drug, was proved to be effective in the tumor therapy [40–43] (noncell cycle specificity). Furthermore, paclitaxel is also a common antitumor drug in the chemotherapy (cell cycle specificity). Finally, we brought the novel 3D-TACs into practical drug screening process to acquire all-round drug effect evaluation of epirubicin and paclitaxel to show the compatibility of the proposed drug screening system with the traditional screening methods.

Screening of different treatment duration: LSCFM images are shown in Fig. 6Ai–iii, and the standardized viabilities analyzed by ImageJ software are shown in Fig. 6C. The data indicated that higher drug concentration exerted higher antitumor effect. The duration of the treatment also had an obvious effect on the viability. Additionally, contrasting 3D and 2D results, the viabilities of 3D models were higher than the ones of 2D models with the same drug concentrations, especially in the middle concentration group (1 μM). This finding verified the defending effect of 3D models deriving from the hydrogel networks. According to the rough screening results, we could determine the drug concentrations in the follow-up screening should be set as 1 μM to 100 μM. Considering the extreme low viability in 100 μM group, we set the drug concentrations in the follow-up drug screening as 0 μM, 1 μM, 5 μM, 10 μM, 25 μM, 50 μM.

VEGF accumulative expression: VEGF, also known as vascular permeability factor (VPF), can promote the increase of vascular permeability and extracellular matrix variability, which is important in tumor vascularization process. As shown in the heat map tested by ELISA method in Fig. 6B, stronger fluctuating of VEGF mass happened on day 4, which demonstrated the gradual trend of accumulative mass with the dose increase. Moreover, it should be noted that the samples in the paclitaxel group showed more colors, which revealed that the VEGF-releasing capability of MDA-MB-231s was gradually limited. For the samples in the epirubicin, when the drug concentrations raised above 1 μM, MDA-MB-231s tended to slow down releasing rate or die.

NAD+ examination for proliferation: Here, we brought the 3D-TACs into the operation of NAD+ examination tested by ELISA method to explore the proliferation behavior of the tumor cells. Figure 6D shows that in all experiment groups, the NAD+ contents obviously decreased with the concentration increasing, confirming that the proliferation capability of MDA-MB-231s was restricted by drugs. Furthermore, in epirubicin group, the NAD+ contents were obviously lower

than the ones in paclitaxel group. The IC50 values of 2D models were 46.09 μM and 27.77 μM, respectively, which were generally lower than the ones of 3D models (47.63 μM and 28.83 μM) as shown in Fig. 6E.

Tumor morphology: The morphologies of the tumor treated by different drugs are shown in Fig. 6F. For the same concentrations, epirubicin showed higher antitumor effect than paclitaxel. The development of tumors began to be restricted at 1 μM in the epirubicin group, whereas at 10 μM in the paclitaxel group. Furthermore, the spreading of the MDA-MB-231s was more obvious in the paclitaxel group. With the treatment of epirubicin, the tumor cells seemed to be killed numerously implied from the restriction of spreading and mitosis according to the signal of phalloidin and DAPI.

Tumor apoptosis by FCM: The apoptosis results summarized by FlowJo are displayed in Fig. 6Ai, ii, and the tumor apoptosis stages proportion are summarized in Fig. 6Bi, ii. In the epirubicin group, the center of cell cluster began moving to early apoptosis cells area at 1 μM and immediately moving to late apoptosis/dead cells area above it. In terms of paclitaxel, from 0 to 25 μM, the move extent was not obvious. Until the concentration was increased to 50 μM the cell cluster began to move to early apoptosis area.

In conclusion, the proposed 3D-TAC in this paper was proved to be feasible to screen antitumor drugs. This system can be perfectly compatible with the conventional drug screening procedure and potential to be utilized in more drug research.

Conclusion

This paper proposed an innovative 3D drug screening system, namely 3D tumor model chip with "layer cake" structure. Precise 3D tumor array could be generated on demand and accurately with the help of the electric field force and motion controlling system. The transparent conductive membrane was introduced as a novel chip basement, which could make it easy for a series of drug examinations and solve the principal problem of electro-assisted printing: charges repelling. In terms of three main factors: building tumor array on demand precisely, providing suitable microenvironment and containing tumor cell functionalization, this tumor chip was demonstrated to be feasible and promising. GelMA was chosen as the ECM deriving from its promising biocompatibility and crosslinking capability. MDA-MB-231s, which own metastasis capability, were encapsulated in 3D-TAC. As a demonstration, we brought the novel 3D-TAC into practical drug screening process to acquire all-round drug effect evaluation of epirubicin and paclitaxel to show the compatibility of the proposed drug screening system with the traditional screening methods, including Calcein-AM/PI (live/dead), tumor morphology, VEGF-accumulative expression, NAD+ examination with CCK-8 for proliferation analysis, half maximal inhibitory concentration IC50 and apoptosis tested by FCM analysis. What's more, as the discussion above, further applications of this system can also focus on establishing "3D-xAC" by encapsulating other kinds of cells or "convenient utilizing" by producing and cryopreserving tumor array membranes on a large scale. We anticipate that the novel 3D-TAC has potential to become a widely applied standard 3D drug screening system for other researchers. It will play an important role in drug screening and can contribute to advance the field of tumor chemotherapy and more biomedical applications.

Acknowledgements This work was sponsored by the National Nature Science Foundation of China (No. U1609207), the National Key Research and Development Program of China (2018YFA0703000) and the Science Fund for Creative Research Groups of the National Natural Science Foundation of China (No. 51521064).

Compliance with ethical standards

Conflict of interest The authors declare that they have no conflict of interest.

Ethical approval This study does not contain any studies with human or animal subjects performed by any of the authors.

References

1. DeVita VT, Chu E (2008) A history of cancer chemotherapy. Cancer Res 68:8643. https://doi.org/10.1158/0008-5472.CAN-07-6611
2. Eglen RM, Randle DH (2015) Drug discovery goes three-dimensional: goodbye to flat high-throughput screening? Assay Drug Dev Technol 13:262–265. https://doi.org/10.1089/adt.2015.647
3. Santo VE, Rebelo SP, Estrada MF, Alves PM, Boghaert E, Brito C (2017) Drug screening in 3D in vitro tumor models: overcoming current pitfalls of efficacy read-outs. Biotechnol J 12:1600505. https://doi.org/10.1002/biot.201600505
4. Liu Y, Shao C, Bian F, Yu Y, Wang H, Zhao Y (2018) Egg component-composited inverse opal particles for synergistic drug delivery. ACS Appl Mater Interfaces 10:17058–17064. https://doi.org/10.1021/acsami.8b03483
5. Wu Z, Yu Y, Zou M, Liu Y, Bian F, Zhao Y (2018) Peanut-inspired anisotropic microparticles from microfluidics. Compos Commun 10:129–135. https://doi.org/10.1016/j.coco.2018.09.007
6. Yu Y, Fu F, Shang L, Cheng Y, Gu Z, Zhao Y (2017) Bioinspired helical microfibers from microfluidics. Adv Mater 29:1605765. https://doi.org/10.1002/adma.201605765
7. Zhang H, Liu Y, Wang J, Shao C, Zhao Y (2019) Tofu-inspired microcarriers from droplet microfluidics for drug delivery. Sci China Chem 62:87–94. https://doi.org/10.1007/s11426-018-9340-y
8. Zhao Y, Gu H, Xie Z, Shum HC, Wang B, Gu Z (2013) Bioinspired multifunctional janus particles for droplet manipulation. J Am Chem Soc 135:54–57. https://doi.org/10.1021/ja310389w
9. Billiet T, Vandenhaute M, Schelfhout J, Van Vlierberghe S, Dubruel P (2012) A review of trends and limitations in hydrogel-rapid proto-

typing for tissue engineering. Biomaterials 33:6020–6041. https://doi.org/10.1016/j.biomaterials.2012.04.050
10. Nam K-H, Smith AST, Lone S, Kwon S, Kim D-H (2014) Biomimetic 3D tissue models for advanced high-throughput drug screening. J Lab Autom 20:201–215. https://doi.org/10.1177/2211068214557813
11. Shin CS, Kwak B, Han B, Park K (2013) Development of an in vitro 3D tumor model to study therapeutic efficiency of an anticancer drug. Mol Pharm 10:2167–2175. https://doi.org/10.1021/mp300595a
12. Cheng R, Yan Y, Liu H, Chen H, Pan G, Deng L, Cui W (2018) Mechanically enhanced lipo-hydrogel with controlled release of multi-type drugs for bone regeneration. Appl Mater Today 12:294–308. https://doi.org/10.1016/j.apmt.2018.06.008
13. Modaresifar K, Hadjizadeh A, Niknejad H (2017) Design and fabrication of GelMA/chitosan nanoparticles composite hydrogel for angiogenic growth factor delivery. Artif Cells Nanomed Biotechnol. https://doi.org/10.1080/21691401.2017.1392970
14. Morales AW, Zhang YS, Aleman J, Alerasool P, Dokmeci MR, Khademhosseini A, Ye JY (2016) Label-free detection of protein molecules secreted from an organ-on-a-chip model for drug toxicity assays. In: SPIE BiOS. SPIE, p 5
15. Nichol JW, Koshy ST, Bae H, Hwang CM, Yamanlar S, Khademhosseini A (2010) Cell-laden microengineered gelatin methacrylate hydrogels. Biomaterials 31:5536–5544. https://doi.org/10.1016/j.biomaterials.2010.03.064
16. Nie J, Gao Q, Wang Y, Zeng J, Zhao H, Sun Y, Shen J, Ramezani H, Fu Z, Liu Z, Xiang M, Fu J, Zhao P, Chen W, He Y (2018) Vessel-on-a-chip with hydrogel-based microfluidics. Small 14:1802368. https://doi.org/10.1002/smll.201802368
17. Shao L, Gao Q, Xie C, Fu J, Xiang M, He Y (2019) Bioprinting of cell-laden microfiber: can it become a standard product? Adv Healthc Mater. https://doi.org/10.1002/adhm.201900014
18. Shao L, Gao Q, Zhao H, Xie C, Fu J, Liu Z, Xiang M, He Y (2018) Fiber-based mini tissue with morphology-controllable GelMA microfibers. Small. https://doi.org/10.1002/smll.201802187
19. Rose BJ, Pacelli S, Haj JA, Dua SH, Hopkinson A, White JL, Rose RF (2014) Gelatin-based materials in ocular tissue engineering. Materials (Basel). https://doi.org/10.3390/ma7043106
20. Xianbin D (2018) 3D bio-printing review. IOP Conf Ser Mater Sci Eng 301:12023
21. Yoon HJ, Shin SR, Cha JM, Lee S-H, Kim J-H, Do JT, Song H, Bae H (2016) Cold water fish gelatin methacryloyl hydrogel for tissue engineering application. PLoS ONE 11:e0163902. https://doi.org/10.1371/journal.pone.0163902
22. Gao Q, Niu X, Shao L, Zhou L, Lin Z, Sun A, Fu J, Chen Z, Hu J, Liu Y, He Y (2019) 3D printing of complex GelMA-based scaffolds with nanoclay. Biofabrication 11:35006. https://doi.org/10.1088/1758-5090/ab0cf6
23. Hassanzadeh P, Kazemzadeh-Narbat M, Rosenzweig R, Zhang X, Khademhosseini A, Annabi N, Rolandi M (2016) Ultrastrong and flexible hybrid hydrogels based on solution self-assembly of chitin nanofibers in gelatin methacryloyl (GelMA). J Mater Chem B 4:2539–2543. https://doi.org/10.1039/C6TB00021E
24. McBeth C, Lauer J, Ottersbach M, Campbell J, Sharon A, Sauer-Budge AF (2017) 3D bioprinting of GelMA scaffolds triggers mineral deposition by primary human osteoblasts. Biofabrication 9:15009. https://doi.org/10.1088/1758-5090/aa53bd
25. Yue K, Trujillo-de Santiago G, Alvarez MM, Tamayol A, Annabi N, Khademhosseini A (2015) Synthesis, properties, and biomedical applications of gelatin methacryloyl (GelMA) hydrogels. Biomaterials 73:254–271. https://doi.org/10.1016/j.biomaterials.2015.08.045
26. Chen X, Bai S, Li B, Liu H, Wu G, Liu S, Zhao Y (2016) Fabrication of gelatin methacrylate/nanohydroxyapatite microgel arrays for periodontal tissue regeneration. Int J Nanomed 11:4707–4718. https://doi.org/10.2147/IJN.S111701
27. Peela N, Sam FS, Christenson W, Truong D, Watson AW, Mouneimne G, Ros R, Nikkhah M (2016) A three dimensional micropatterned tumor model for breast cancer cell migration studies. Biomaterials 81:72–83. https://doi.org/10.1016/j.biomaterials.2015.11.039
28. Yan X, Zhou L, Wu Z, Wang X, Chen X, Yang F, Guo Y, Wu M, Chen Y, Li W, Wang J, Du Y (2019) High throughput scaffold-based 3D micro-tumor array for efficient drug screening and chemosensitivity testing. Biomaterials 198:167–179. https://doi.org/10.1016/j.biomaterials.2018.05.020
29. Cui X, Dean D, Ruggeri ZM, Boland T (2010) Cell damage evaluation of thermal inkjet printed Chinese hamster ovary cells. Biotechnol Bioeng 106:963–969. https://doi.org/10.1002/bit.22762
30. Barrero A, Loscertales IG (2006) Micro- and nanoparticles via capillary flows. Annu Rev Fluid Mech 39:89–106. https://doi.org/10.1146/annurev.fluid.39.050905.110245
31. Fernández de la Mora J (2006) The fluid dynamics of Taylor Cones. Annu Rev Fluid Mech 39:217–243. https://doi.org/10.1146/annurev.fluid.39.050905.110159
32. Xie M, Gao Q, Zhao H, Nie J, Fu Z, Wang H, Chen L, Shao L, Fu J, Chen Z, He Y (2019) Electro-assisted bioprinting of low-concentration GelMA microdroplets. Small 15:1–10. https://doi.org/10.1002/smll.201804216
33. Plodinec M, Loparic M, Monnier CA, Obermann EC, Zanetti-Dallenbach R, Oertle P, Hyotyla JT, Aebi U, Bentires-Alj M, Lim RYH, Schoenenberger C-A (2012) The nanomechanical signature of breast cancer. Nat Nanotechnol 7:757–765. https://doi.org/10.1038/nnano.2012.167
34. Zhao X, Liu S, Yildirimer L, Zhao H, Ding R, Wang H, Cui W, Weitz D (2016) Injectable stem cell-laden photocrosslinkable microspheres fabricated using microfluidics for rapid generation of osteogenic tissue constructs. Adv Funct Mater 26:2809–2819. https://doi.org/10.1002/adfm.201504943
35. Deryugina EI, Quigley JP (2006) Matrix metalloproteinases and tumor metastasis. Cancer Metastasis Rev 25:9–34. https://doi.org/10.1007/s10555-006-7886-9
36. Jung HY, Fattet L, Yang J (2015) Molecular pathways: linking tumor microenvironment to epithelial-mesenchymal transition in metastasis. Clin Cancer Res 21:962. https://doi.org/10.1158/1078-0432.CCR-13-3173
37. Liang C, Xu L, Song G, Liu Z (2016) Emerging nanomedicine approaches fighting tumor metastasis: animal models, metastasis-targeted drug delivery, phototherapy, and immunotherapy. Chem Soc Rev 45:6250–6269. https://doi.org/10.1039/C6CS00458J
38. Polacheck WJ, Zervantonakis IK, Kamm RD (2013) Tumor cell migration in complex microenvironments. Cell Mol Life Sci 70:1335–1356. https://doi.org/10.1007/s00018-012-1115-1
39. Wagenblast E, Soto M, Gutiérrez-Ángel S, Hartl CA, Gable AL, Maceli AR, Erard N, Williams AM, Kim SY, Dickopf S, Harrell JC, Smith AD, Perou CM, Wilkinson JE, Hannon GJ, Knott SRV (2015) A model of breast cancer heterogeneity reveals vascular mimicry as a driver of metastasis. Nature 520:358. https://doi.org/10.1038/nature14403https://www.nature.com/articles/nature14403%23supplementary-information
40. Aramaki T, Moriguchi M, Bekku E, Asakura K, Sawada A, Endo M (2013) Comparison of epirubicin hydrochloride and miriplatin hydrate as anticancer agents for transcatheter arterial chemoembolization of hepatocellular carcinoma. Hepatol Res 43:475–480. https://doi.org/10.1111/j.1872-034X.2012.01100.x
41. Lovitt CJ, Shelper TB, Avery VM (2015) Evaluation of chemotherapeutics in a three-dimensional breast cancer model. J Cancer Res Clin Oncol 141:951–959. https://doi.org/10.1007/s00432-015-1950-1

42. Lu CT, Zhao YZ, Wu Y, Tian XQ, Li WF, Huang PT, Li XK, Sun CZ, Zhang L (2011) Experiment on enhancing antitumor effect of intravenous epirubicin hydrochloride by acoustic cavitation in situ combined with phospholipid-based microbubbles. Cancer Chemother Pharmacol 68:343–348. https://doi.org/10.1007/s00280-010-1489-4

43. Zhang L, Li G, Gao M, Liu X, Ji B, Hua R, Zhou Y, Yang Y (2016) RGD-peptide conjugated inulin-ibuprofen nanoparticles for targeted delivery of Epirubicin. Colloids Surfaces B Biointerfaces 144:81–89. https://doi.org/10.1016/j.colsurfb.2016.03.077